Chinese Chemical Letters 34 (2023) 107886

Contents lists available at ScienceDirect

Chinese Chemical Letters

journal homepage: www.elsevier.com/locate/cclet

Organic carboxylate-assisted engineering for fabricating Fe, N co-doped porous carbon interlinked carbon nanotubes towards boosting the oxygen reduction reaction for Zn-air batteries

Jing Zhang[1], Ye Chen[1], Miao Tian, Tianfang Yang, Fengxian Zhang, Guangrui Jia*, Xupo Liu*

School of Materials Science and Engineering, Henan Normal University, Xinxiang 453007, China

ARTICLE INFO

Article history:
Received 29 August 2022
Revised 24 September 2022
Accepted 4 October 2022
Available online 13 October 2022

Keywords:
Oxygen reduction reaction
Organic carboxylate
Active point-conductive line-active point
Self-catalyzed effect
Zn-air battery

ABSTRACT

Fe-N_x sites have been identified as core descriptors for Fe-N/C based oxygen reduction reaction catalysts. However, the low density and less utilization of Fe-N_x sites render these catalysts with inefficient catalytic performance. Herein, we develop an organic carboxylate-assisted engineering to construct Fe, N co-doped porous carbon interlinked carbon nanotubes (Fe/N-CCNTs) with high-density and sufficiently exposed Fe-N_x sites based on self-catalyzed effect. The existing forms of Fe include Fe-imidazole configuration and coordination with unsaturated Zn sites *via* organic carboxylate as linkers, leading to high-density Fe-N_x sites after pyrolysis. Besides, hexatomic carbon rings of organic carboxylate lower cyclization energy barrier for CNT formation, resulting in CNTs interlinked with separated active sites through "active point-conductive line-active point" connections. The optimal sample (Fe-BOAc-PNC) exhibits the onset potential of 0.93 V (*vs.* RHE) and half-wave potential of 0.84 V in alkaline solution. The liquid-state Zn-air battery (ZAB) employing Fe-BOAc-PNC generates large power density (160 mW/cm^2) and stability over 160 h. Moreover, the assembled flexible ZAB displays superb power density of 93 mW/cm^2 with robust flexibility. This work provides an insightful perspective for designing Fe-N/C catalysts with high-density and sufficiently exposed active sites for energy storage application.

Rechargeable Zn-air batteries (ZABs) have gained wide attentions as a variety of new-type energy storage devices because of their high theoretical energy density, environmentally friendly, low price, as well as intrinsic safety [1,2]. However, the oxygen reduction reaction (ORR), which is the air cathodes of ZABs, suffers from the sluggish kinetics involving multistep and multielectron redox [3–7]. Despite the excellent ORR activity of platinum (Pt)-based materials, the scarce reserves, prohibitive cost and humble stability limit their large-scale application [8–11]. In this regard, putting more efforts to develop inexpensive, high-efficiency and robust non-precious metal catalysts (NPMCs) is highly desirable. Among NPMCs, the transition metal and nitrogen co-doped carbon (M-N/C) catalysts show promising ORR catalytic activity because M-N_x sites have the capacity of offering energetically favorable adsorption sites for ORR intermediates (O*, OH* and OOH*), thereby promoting the direct 4-electron process [12]. Iron-based catalytic materials with high spin state of Fe ions and abundant Fe-N_x local charge accelerate the electron transfer between Fe sites and adsorbed reactants/intermediates, resulting in enhanced ORR performance [13].

The Fe-N/C catalysts with dense Fe-N_x active sites can effectively optimize O_2 adsorption towards four-electron ORR according to density functional theory (DFT) calculations. Recent spectroscopic researches reveal that adjusting Fe-N_x configuration can effectively improve the ORR activity [14–19]. Moreover, the 3-dimensional (3D) hierarchically porous architecture with open channels is beneficial for maximizing the accessibility of active Fe-N_x sites [20]. Therefore, it is important to prepare high-density Fe-N_x sites in a carbon matrix for excellent ORR performance, meanwhile 3D frameworks with porous channels are applied for adequate exposure of active sites and smooth mass transfer. Metal-organic frameworks (MOFs) possess some specific characteristics of high specific surface area, good design ability, and easily functionalized, which can not only construct 3D porous structure but also satisfy the requirements of Fe-N/C compositions [21–23].

Herein, the Fe, N co-doped porous carbon interlinked carbon nanotubes (Fe/N-CCNTs) derived from zeolitic-imidazolate-framework-8 (ZIF-8) have been prepared based on the self-catalyzed effect through the organic carboxylate-assisted engi-

* Corresponding authors.
E-mail addresses: jgr@htu.edu.cn (G. Jia), liuxupo@htu.edu.cn (X. Liu).
[1] These authors contributed equally to this work.

https://doi.org/10.1016/j.cclet.2022.107886
1001-8417/

neering. The organic carboxylate can coordinate with unsaturated Zn sites and Fe ions to improve the Fe doping content, resulting in high-density Fe-N_x sites through high temperature treatment. Meanwhile, the hexatomic carbon rings in organic carboxylate can efficiently lower the cyclization energy barrier during CNT formation process, which ensures smooth diffusion of reactants and full exposure of active sites. In addition, Fe/Fe_3C nanoparticles (NPs) anchored in carbon skeletons are profitable for adjusting the electronic structure of adjacent carbon surfaces to improve the corrosion resistance. The "active point-conductive line-active point" connections between CNTs and the active sites offer high exposure of active sites, interconnected mass diffusion channels and interlinked electron highways. Thus, the optimal sample (Fe-BOAc-PNC) exhibits excellent electrocatalytic ORR performance ($E_{onset} = 0.93$ V, $E_{1/2} = 0.84$ V, $j_K = 4.90$ mA/cm^2) in alkaline solution. The liquid ZAB assembled with Fe-BOAc-PNC as cathode generates a high maximum power density (160 mW/cm^2) and a high specific capacity (812 mAh/g) together with excellent long-term rechargeable stability over 220 h. Besides, the flexible solid-state ZAB employing Fe-BOAc-PNC as air cathode generates a high maximum power density (94 mW/cm^2) and robust flexibility and stability, demonstrating a promising application in wearable electronic devices.

All the chemicals used in the synthesis of catalysts were analytical purity and no further purification was made. 2-Methylimidazole ($C_4H_6N_2$, AR), sodium acetate (CH_3COONa, AR), zinc nitrate hexahydrate ($Zn(NO_3)_2{\cdot}6H_2O$, AR), sodium benzoate ($C_7H_5NaO_2$, AR), ferric chloride hexahydrate ($FeCl_3{\cdot}6H_2O$), silicon dioxide (SiO_2, AR), zinc acetate ($Zn(Ac)_2$, AR), potassium thiocyanate (KSCN, AR), potassium hydroxide (KOH, AR), zinc oxide (ZnO, AR), acrylic acid ($C_3H_4O_2$, AR), *N*,*N*'-methylenebisacrylamide ($C_7H_{10}N_2O_2$, AR), methanol (CH_3OH, AR) and polytetrafluoroethylene dispersion (PTFE, 60 wt%) were purchased from Aladdin. Hydrofluoric acid (HF, 40 wt%) was obtained from Yantai Shuangshuang Chemical Co., Ltd. Nafion solution (5 wt%) and Pt/C (20 wt%) were acquired from Shanghai Hesen Electric Appliance Co., Ltd. Deionized water was employed with a specific resistance (18.25 MΩ cm).

2-Methylimidazole (6.5 g) was dispersed into methanol (100 mL) with ultrasonic treatment to gain solution A. The solution B is consistent of $Zn(NO_3)_2{\cdot}6H_2O$ (3 g) and methanol (50 mL). Next, solution B was fast poured into solution A, and the mixed solution was stirring for a period of time (24 h) at room temperature. The obtained samples were under centrifugation, washed with methanol for three times, followed by drying under vacuum at 60 °C overnight. The obtained powders were ZIF-8 precursors. ZIF-8 (0.8 g) and SiO_2 (0.4 g) were added into methanol (30 mL) to acquire solution C by ultrasonication for 30 min. Afterwards, the solution C was stirring for 12 h at room temperature. The acquired precipitates were collected with centrifugation at 10,000 r/min and cleaned with methanol for three times. The obtained product was dried at 80 °C under vacuum overnight, which was noted as ZIF-8@SiO_2. Accordingly, other precursors were also prepared by the similar approach except the solution C. The sample derived from solution C with 0.8 g ZIF-8, 0.4 g SiO_2 and 0.27 g $FeCl_3{\cdot}6H_2O$ was noted as ZIF-8@SiO_2@Fe. The sample derived from solution C with 0.8 g ZIF-8, 0.4 g SiO_2, 0.27 g $FeCl_3{\cdot}6H_2O$ and 0.328 g CH_3COONa was labeled as ZIF-8@SiO_2@Fe-OAc. The sample derived from solution C with 0.4 g SiO_2, 0.27 g $FeCl_3{\cdot}6H_2O$ and 0.576 g $C_7H_5NaO_2$ was named as ZIF-8@SiO_2@Fe-BOAc. The obtained ZIF-8@SiO_2 precursor was treated at high temperature at 900 °C under nitrogen atmosphere for 2 h (5 °C/min). Then, the black powders were dispersed into HF solution (15 wt%) for 12 h to dissolve excess metals and impurities, followed by cleaning with deionized water and drying in a vacuum at 80 °C. As-formed sample was named as PNC. Similarly, ZIF-8@SiO_2@Fe, ZIF-8@SiO_2@Fe-OAc, and ZIF-8@SiO_2@Fe-BOAc processed by the same procedure were denoted as Fe-PNC, Fe-OAc-PNC, and Fe-BOAc-PNC, respectively.

The micromorphology and structure were investigated using field emission scanning electron microscope (FE-SEM, JEOL SU8010) and high-resolution field emission transmission electron microscope (TEM, F200X). The X-ray energy-dispersive spectrometer (EDS) was applied to observe element distributions of the catalysts. The powder X-ray diffraction (XRD) patterns were carried out by Bruker D8 with Cu-Kα source ($\lambda = 0.154$ nm). An Autosorb Station iQ2 was used to measure Brunauer-Emmett-Teller (BET) surface area based on the nitrogen adsorption/desorption isotherm technique at 77 K. X-ray photoelectron spectra (XPS) were obtained on ESCALAB250Xi equipment with monochromatic Al Kα. The content of Fe was verified through an ELAN DRC-e inductively coupled plasma mass spectrometer (ICP-MS). Fourier transform infrared spectra (FT-IR) were investigated using the Thermo Nicolet Corporation NEXUS apparatus. The hydrophilicity of samples was calculated by KRüSS DSA25. The thermogravimetric analyses (TGA) thermal analyzer (NETZSCH STA449F3) at 1000 °C under nitrogen atmosphere was conducted to obtain the weight losses of samples.

The electrochemical test was performed in a typical three-electrode system using a CHI660E electrochemical workstation. A catalyst-coated glassy carbon electrode, Hg/HgO electrode (in saturated KCl solution) and Pt foil (1 cm^2) were used as the working electrode, the reference and the counter electrodes, respectively. The electrolyte was 0.1 mol/L KOH solution. To prepare the homogeneous dispersion, the as-prepared catalyst (1 mg) was dispersed in a mixed solution of ethanol (95 μL), Nafion solution (10 μL, 5 wt%) and deionized water (95 μL), followed by ultrasonication for 1 h. Next, the homogeneous dispersion (7/12/20 μL) was pipetted onto the glassy carbon electrode surface (diameter 3/4/5 mm). The mass loadings of samples and Pt/C catalyst were about 0.5 mg/cm^2 and 0.2 mg/cm^2, respectively.

Cyclic voltammetry (CV) measurements were performed at a scan rate of 10 mV/s in N_2- or O_2-saturated 0.1 mol/L KOH solution. For linear sweep voltammetry (LSV) tests, the rotating ring disk electrode (RRDE) measurements were conducted at a rotation rate of 1600 rpm in N_2- or O_2-saturated 0.1 mol/L KOH electrolyte (deducting the N_2 background) at a sweep rate of 10 mV/s. The rotating disk electrode (RDE) tests in 0.1 mol/L KOH solution saturated in N_2 or O_2 were carried out with different rotating rates from 400 rpm to 2025 rpm, and the scan rate is 10 mV/s.

The potentials were converted to the reversible hydrogen electrode (RHE) based on the following equation:

$$E_{RHE} = E_{Hg/HgO} + 0.059\ pH + E^{\theta}_{Hg/HgO} \quad (1)$$

where $E_{Hg/HgO}$ is calculated using Hg/HgO as the reference electrode, $E^{\theta}_{Hg/HgO}$ (saturated with 1 mol/L KOH solution) is 0.098 V.

The Koutecky-Levich (K-L) plots were analyzed by RDE test at different sweep rates. The electron transfer numbers were measured through the slopes of linear lines according to the K-L equation:

$$\frac{1}{j} = \frac{1}{j_L} + \frac{1}{j_K} = \frac{1}{B\omega^{1/2}} + \frac{1}{j_K} \quad (2)$$

where j refers to the measured current density, j_L and j_K are diffusion- and kinetic-limited current densities. ω is corresponding to the angular velocity of the disk, and B is calculated from the slope of K-L plot using Levich equation:

$$B = 0.2nFC_0D_0^{2/3}\upsilon^{-1/6} \quad (3)$$

where n represents the electron transfer number, F refers to the Faraday constant (F = 96,485 C/mol), C_0 and D_0 are bulk concentration of O_2 ($C_0 = 1.2 \times 10^{-3}$ mol/cm^3 in 0.1 mol/L KOH) and diffusion coefficient of O_2 ($D_0 = 1.9 \times 10^{-5}$ cm^2/s in 0.1 mol/L KOH), respectively. υ is the kinematic viscosity of the electrolyte ($\upsilon = 0.01$ cm^2/s).

The electron transfer number (n) and the peroxide percentage (H_2O_2%) can be calculated by the following equations:

$$H_2O_2\% = 200I_r/N(I_d + I_r/N) \quad (4)$$

$$n = 4I_d/(I_d + I_r/N) \quad (5)$$

where I_r and I_d are the ring and disk currents, respectively, and N is the ring collection efficiency ($N = 0.37$).

The electrochemically active surface area (ECSA) was determined according to $A = C_{dl}/C_s$, where C_{dl} and C_s represent the double layer capacitance and specific capacitance, respectively. The C_{dl} was calculated with various sweep of 5, 10, 15, 20, 30, 40 and 50 mV/s from 1.065 V to 1.165 V.

The stability of catalysts was evaluated by CV curves with accelerated CV measurement with a sweep rate of 50 mV/s from 0.265 V to 0.865 V. The methanol tolerance of catalysts was studied by comparing the CV curves before and after methanol addition (1 mL). Poisoning experiment was executed in O_2-saturated solutions with addition of 10 mmol/L KSCN. Electrochemical impedance spectroscopy (EIS) tests were carried out from 100 kHz to 0.01 Hz with an AC voltage with 5 mV amplitude.

The liquid ZAB was assembled using a catalyst-coated carbon paper as the air cathode, a polished Zn foil as the anode, and the mixed solution of 6.0 mol/L KOH and 0.2 mol/L $Zn(Ac)_2$. To obtain the catalyst ink, the as-synthesized catalyst (2.5 mg) was dispersed isopropyl alcohol (200 μL), PTFE dispersion (8 μL, 20 wt%) and Nafion solution (16 μL, 5 wt%). The catalyst-coated carbon paper with the loading of 2 mg/cm^2 was dried naturally. The Pt/C catalyst (20 wt%) was prepared with the same loading of 2 mg/cm^2 as control. The electrochemical workstation (CHI660E) was performed to obtain the discharge/charge plots. The polarization curve measurements based on steady-state LSV were conducted at the sweep rate of 5 mV/s. The power density (P) of the ZAB was calculated by $P = IV$, among which V and I were voltage and discharge current density, respectively. The charge-discharge cycling measurements were conducted at a scan rate of 5 mA/cm^2 with per cycling interval for 10 min. The specific capacity (C) was determined from $C = It/m$, where m referred to the mass of consumed Zn foil, I was the discharge current and t represented the discharge time.

A polished Zn foil, solid-state electrolyte and the air-electrode were attached successively to form a flexible solid-state ZAB. An electrode composite substrate (hydrophobic carbon paper + waterproof film + nickel foam) coated with a certain amount of Fe-BOAc-PNC or commercial Pt/C catalyst was fabricated by drop-casting. The catalyst preparation and mass loading of flexible ZAB were the same as those of the liquid ZAB. The preparation method of gel polymer electrolyte was as follows: Firstly, acrylic acid (0.8 g) and *N,N*'-methylenebisacrylamide (0.12 g) are dispersed into 8 mL mixed solution containing with 0.25 mol/L ZnO and 11.25 mol/L KOH, following by starting to polymerize when 120 μL saturated $K_2S_2O_4$ was added. The discharge/charge tests were conducted using the electrochemical workstation (CHI660E). The galvanostatic cycling measurements were conducted at the current density of 1 mA/cm^2 with per cycling interval of 10 min (5 min for charging and 5 min for discharging). The specific capacity was determined at 5 mA/cm^2 and normalized to the mass of consumed Zn.

An organic carboxylate-assisted engineering has been adopted to construct Fe/N-CCNTs. As depicted in Scheme 1a, the synthesis process of Fe/N-CCNTs consists of two main processes: the introduction of Fe in ZIF-8 precursors with SiO_2 and high temperature pyrolysis (900 °C). When Fe ions are directly incorporated into ZIF-8, they are introduced with Fe-imidazole coordination [24,25]. It is gratifying that Fe ions are additionally doped with the existence of carboxylate, in which unsaturated coordinated Zn sites and Fe ions

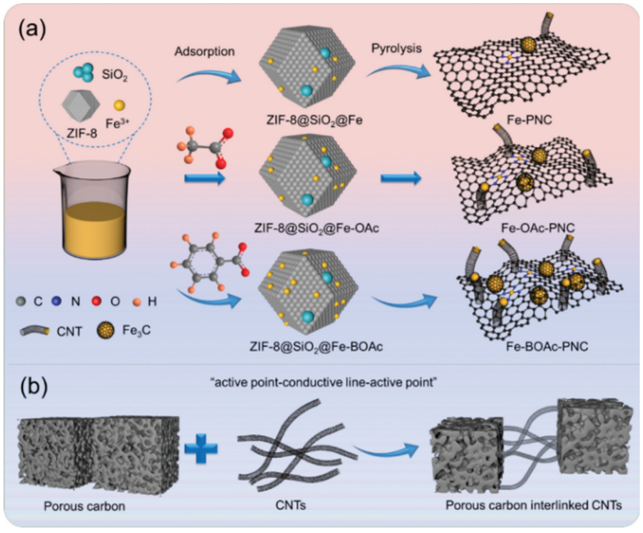

Scheme 1. (a) Illustration of the synthetic strategy of Fe/N-CCNTs. (b) Schematic diagram for Fe/N-CCNTs with "active point-conductive line-active point" connections.

can be linked. Fe ions are more inclined to be introduced with carboxylate as a linker instead of the direct substitution of Zn ions with Fe ions when carboxylate is present [26]. Thus, with the addition of organic carboxylate, the existing forms of Fe ions include Fe-imidazole configuration and the coordination with unsaturated Zn sites *via* organic carboxylate as linkers, leading to high density of Fe-N_x active sites after pyrolysis. It is reported that the existence of six-atom carbon rings in sodium benzoate is capable of lowering the cyclization energy barrier during the CNT formation process, which is conducive to the generation of CNTs, providing rich transport channels and promoting the exposure of effective active sites [27,28]. Besides, the Fe/Fe_3C NPs anchored in nitrogen-doped carbon can effectively adjust the electronic structure of adjacent carbon surfaces, which can enhance the stability and corrosion resistance of carbon catalysts. Scheme 1b depicts that CNTs are selected as highly conductive lines and Fe-N_x sites are considered as active centers. Attributed to "active point-conductive line-active point" connections, the Fe sites are sufficiently exposed and interlinked by CNTs, thus facilitating interfacial charge transport, and efficient utilization of active sites [29].

The morphology of Fe/N-CCNTs catalysts is investigated by SEM and TEM techniques. As depicted in Fig. S1 (Supporting information), PNC displays a polyhedral shape similar to ZIF-8. Accompanying with the addition of Fe salts, the polyhedron shape collapses and CNTs are formed *in situ*. In fact, the Fe species are firstly reduced to produce Fe nanoparticles during pyrolysis. In the following, carbon atoms continuously diffuse and happen to reach the surface of Fe nanoparticles. Accordingly, CNTs are *in situ* formed based on the self-catalyzed effect [30]. As shown in Fig. 1a, ZIF-8@SiO_2@Fe-BOAc precursor remains a typical polyhedral morphology with stacked SiO_2 nanospheres. After high temperature pyrolysis and HF acid etching, SEM image of Fe-BOAc-PNC in Fig. 1b displays the structure of hierarchically porous carbon interlinked CNTs. The fracture of polyhedron structure may result from the reduction of Fe^{3+} to Fe NPs and the oxidation of carbon to CO or CO_2. Meanwhile, Zn ions are reduced by carbon to become Zn metals, nanopores in the carbon layers are formed with the evaporation of metal Zn at high temperature. The TEM images for Fe-BOAc-PNC verify the existence of porous CNT-anchored carbon network (Figs. 1c and d), which can promote smooth mass transport and exposure of the active sites. Figs. 1e and f exhibit that two visible fringes of 0.20 and 0.34 nm are correspond to Fe_3C (220) and graphitic carbon (002), suggesting that Fe_3C NPs are encap-

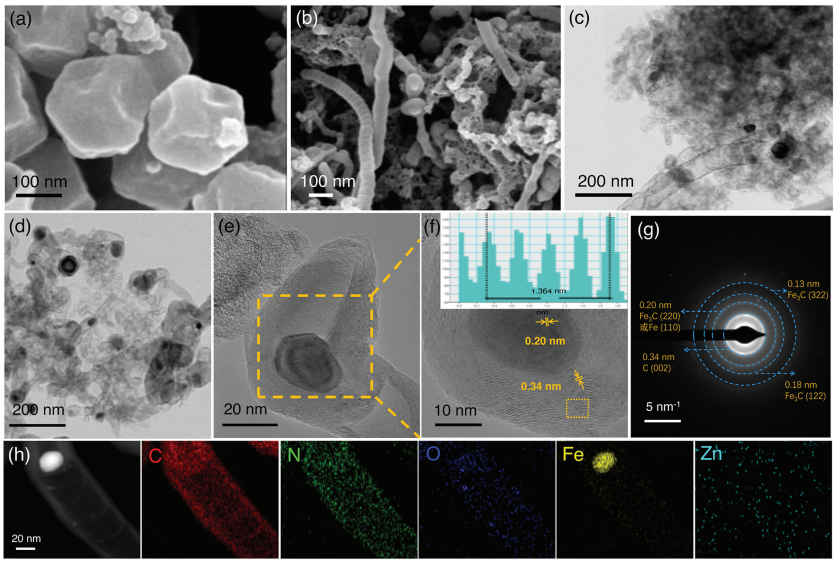

Fig. 1. SEM images of (a) ZIF-8@SiO_2@Fe-BOAc and (b) Fe-BOAc-PNC. (c, d) TEM and (e, f) HR-TEM images of Fe-BOAc-PNC. (g) SAED pattern of Fe-BOAc-PNC. (h) HAADF-STEM and the corresponding elemental mappings.

sulated in graphitic carbon layers. The carbon nanostructure can not only be beneficial to electrolyte infiltration but also prevent Fe_3C NPs from dissolving [31]. The ring-like selected region electron diffraction (SAED) pattern effectively proves Fe-containing NPs on Fe-BOAc-PNC (Fig. 1g). The parallel fringe spacing of 0.34 nm is corresponded to graphitic carbon (002), the fringe spacings of 0.18 nm and 0.13 nm are assigned to Fe_3C (122) and Fe_3C (322), respectively. Besides, the parallel fringe with interplanar spacing of 0.20 nm is attributed to Fe_3C (220) or Fe (110), matching well with HR-TEM results. EDS mapping suggests that CNTs have C, N, O, Zn elements and Fe NPs (Fig. 1h).

XRD patterns are analyzed to illuminate the compositions of Fe/N-CCNTs. The diffraction peaks of as-prepared precursors are similar to ZIF-8 (Fig. S2 in Supporting information). After high temperature pyrolysis and acid etching, a broad diffraction peak at approximately 21.3° is attributed to graphite carbon (002) for PNC (Fig. 2a). With the introduction of metal salt, the increasing peaks positioned at 26.4°, 43.7°, 51.8°, 75.4° are well indexed to the patterns of Fe_3C (JCPDS No. 35-0772) and a diffraction peak at 44.7° is corresponded to Fe (JCPDS No. 06-0696), suggesting the generation of multicomponent iron catalyst for Fe-PNC, Fe-OAc-PNC and Fe-BOAc-PNC. Raman analysis is conducted to evaluate the defect degree for carbon materials. The typical disordered carbon (D bands) and sp^2-hybridized graphitic carbon (G bands) are located at 1348 cm^{-1} and 1568 cm^{-1}, respectively (Fig. 2b) [32]. The intensity ratio of the D-band to the G-band ($I_D/I_G = 0.87$) for Fe-BOAc-PNC, which is smaller than those of PNC ($I_D/I_G = 1.31$), Fe-PNC ($I_D/I_G = 0.98$) and Fe-OAc-PNC ($I_D/I_G = 1.02$), reflecting a high degree of graphitization. The high degree of graphitization is conducive to enhancing carbon corrosion resistance, thereby improving the stability of carbon catalysts [33,34]. The pyrolysis process of the as-prepared samples is monitored by TGA in N_2 atmosphere (Fig. 2c). ZIF-8@SiO_2@Fe-BOAc starts to degrade at about 80 °C and presents a dramatic weight loss of about 20% at around 245 °C. The total weight loss of ZIF-8@SiO_2@Fe-BOAc reaches 53 wt% at 1000 °C, illustrating lower thermal stability than other precursors. These results imply that ZIF-8@SiO_2@Fe-BOAc is easily decomposable, which will generate gaseous products and form porous framework during pyrolysis. N_2 adsorption-desorption isotherms and pore size distributions are obtained to evaluate the textural properties of catalysts in Figs. 2d and e. All catalysts contain the type-IV isotherms with a distinct H1 hysteresis loop at high relative pressure, indicating the porosity of produced catalysts. The BET surface areas of Fe-PNC, Fe-OAc-PNC and Fe-BOAc-PNC are 628.1 m^2/g, 484.0 m^2/g and 677.3 m^2/g, respectively, which is smaller than PNC (1310.3 m^2/g). This is caused by iron species blocking the pores on the surface of the carbon substrate. Moreover, these samples have characteristic mesopores located at around ~16 nm and ~26 nm, which are conductive to facilitating fast diffusion of reactants and active site exposure during ORR process. The chemical bonds of Fe/N-CCNTs catalysts are identified by FT-IR measurement (Fig. 2f). The -OH bond at about 3437 cm^{-1} attribute to the water and oxygen functional groups [35]. The peak located at 882 cm^{-1} for Fe-PNC, Fe-OAc-PNC and Fe-BOAc-PNC is attributed to the Fe-N bonds, suggesting iron atoms are successfully introduced. The peaks located at 2924 and 1384 cm^{-1} are raised from C–H bonds. Peaks for Fe-BOAc-PNC located at 1456 cm^{-1}, 1626 cm^{-1}, 1086 cm^{-1} and 1036 cm^{-1} are raised from C-N, C=O, C-O and C-O-C, respectively. Nitrogen and oxygen doping has been observed in the materials, which is expected to improve the surface wettability of carbon materials. The water contact angles of PNC, Fe-PNC, Fe-OAc-PNC and Fe-BOAc-PNC are illustrated in Fig. S3 (Supporting infomation). The contact angle of Fe-BOAc-PNC is 5.8°, much smaller than other samples. The stronger hydrophilicity can shorten the distance of reactants and catalyst, thereby promoting the mass transfer process [9,36].

XPS tests are further performed to identify chemical compositions of prepared catalysts. The survey XPS pattern exhibits that Fe-BOAc-PNC has C, N, O, Fe and Zn (Fig. 2g). ICP-MS results illustrate Fe contents of Fe-PNC, Fe-OAc-PNC and Fe-BOAc-PNC are about 1.78 wt%, 2.43 wt% and 2.63 wt%, respectively (Table S1 in Supporting information), suggesting that carboxylate linkers are profitable for improving the Fe contents. The four peaks of C 1s spectrum for Fe-BOAc-PNC located at 284.5 eV, 285.1 eV, 286.0 eV and 288.9 eV are corresponding to C-C sp^3, C-C sp^2, C-N and C=O/C=N (Fig. 2h). Moreover, the O 1s spectrum of Fe-BOAc-PNC exhibits three characteristic peaks: Fe-O/Zn-O (530.7 eV), C=O (532.2 eV) and C-OH/C-O-C (533.6 eV), suggesting that carbon surfaces contain oxygen species (Fig. 2i) [37]. Fig. 2j depicts that the Fe 2p spectrum for Fe-BOAc-PNC can be deconvoluted into three doublets: Fe^{3+}, Fe^{2+} and Fe^0. The binding energies of 712.2 eV and 725.8 eV are corresponding to Fe^{3+} $2p_{3/2}$ and Fe^{3+} $2p_{1/2}$, respectively. The characteristic peaks located at 710.2 and 723.8 eV belong to Fe^{2+} $2p_{3/2}$ and Fe^{2+} $2p_{1/2}$. Besides, the typical peaks sit-

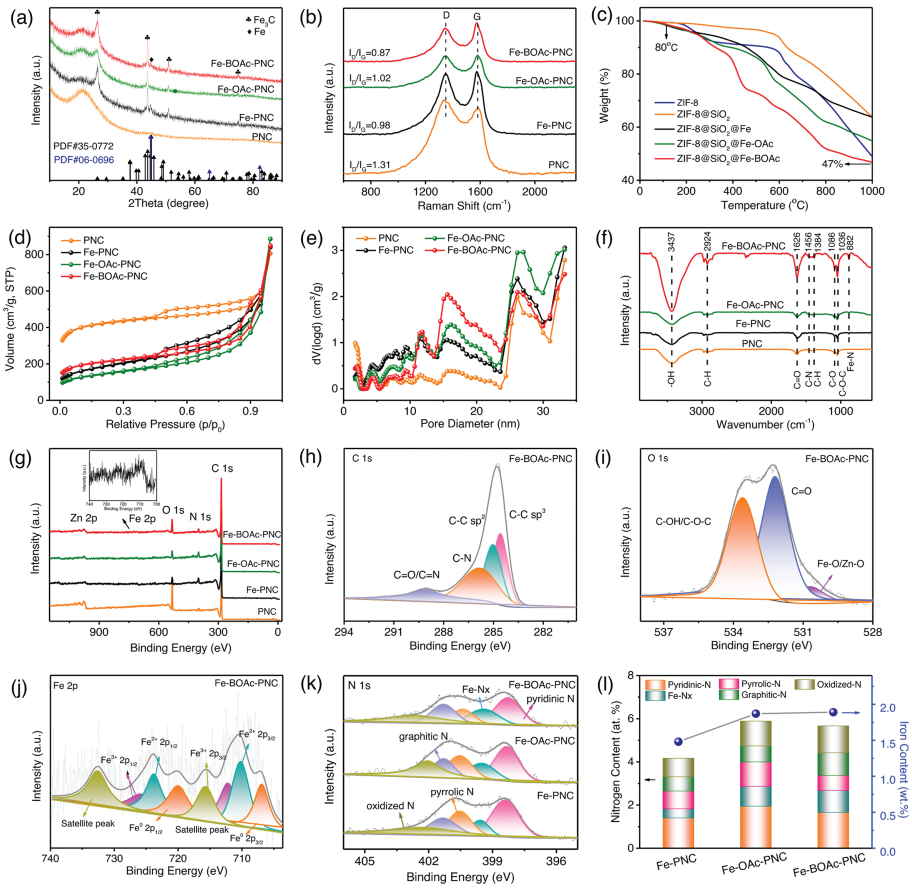

Fig. 2. (a) XRD patterns. (b) Raman spectra. (c) TGA curves. (d) N_2 adsorption-desorption isotherms. (e) Pore-size distributions. (f) FT-IR spectra. (g) XPS survey spectra. (h) C 1s, (i) O 1s, (j) Fe 2p, and (k) N 1s XPS spectra. (l) Contents of N species and Fe.

uated at 706.9 eV and 720.0 eV are assigned to Fe^0 $2p_{3/2}$ and Fe^0 $2p_{1/2}$. Meanwhile, the convolutions of N 1s spectra for Fe-PNC, Fe-OAc-PNC and Fe-BOAc-PNC exhibit five forms at approximately 398.3, 399.5, 400.4, 401.3 and 402.6 eV, which are corresponding to pyridinic N, Fe-N_x, pyrrolic N, graphitic N and oxidized N (Fig. 2k). Fig. 2l and Table S1 (Supporting information) show that Fe contents for Fe-OAc-PNC and Fe-BOAc-PNC are 1.87 wt% and 1.89 wt% by XPS analysis, respectively, which are higher than that of Fe-PNC (1.48 wt%), matching well with the results of ICP-MS. Moreover, Fe-BOAc-PNC exhibits a higher Fe-N_x contents of 1.02 at% and graphitic N contents of 1.04 at% than Fe-PNC and Fe-OAc-PNC (Table S2 in Supporting information). Previous DFT calculations have shown that Fe-N_x active sites can affect binding energy of reaction species and electronic structure of Fe center, resulting in an increase in electrochemical activity [38,39]. In addition, graphite N can reduce the adsorption energy of oxygen, thus significantly increase the limiting current density during ORR process [40,41].

Electrochemical methods are conducted to measure electrochemical performance of catalysts. The CV measurements are firstly conducted in N_2- or O_2-saturated 0.1 mol/L KOH solution. Fig. 3a illustrates that the catalysts have no reduction peak in N_2 saturated electrolyte, while there are strong peaks in O_2 saturated electrolyte. Compared with other catalysts, Fe-BOAc-PNC exhibits a more positive peak potential of 0.85 V, implying its excellent ORR activity. Next, Fig. 3b illustrates that the RRDE measurements are carried out in 0.1 mol/L O_2-saturated KOH media when the rotation speed is 1600 rpm. Similar to the trend in CV curves, Fe-BOAc-PNC delivers a more excellent half-wave potential of 0.84 V compared to other samples, which is equivalent to the benchmark Pt/C (0.84 V). Usually, the onset potentials (E_{onset}), half-wave potentials ($E_{1/2}$) and kinetic current density (j_K) are regarded as three important criterion indexes for ORR. As illustrated in Fig. 3c, Fe-BOAc-PNC possesses the highest E_{onset} (0.93 V), $E_{1/2}$ (0.84 V) and j_K (4.90 mA/cm^2) than those of PNC (0.90 V, 0.81 V, 2.51 mA/cm^2), Fe-PNC (0.89 V, 0.80 V, 2.02 mA/cm^2), and Fe-OAc-PNC (0.87 V, 0.77 V, 1.10 mA/cm^2), which is close to the benchmark Pt/C (0.97 V, 0.84 V, 5.20 mA/cm^2), implying its outstanding ORR performance. The RRDE results reveal that an average n value (3.9) and a H_2O_2 yield (~5%) are achieved for Fe-BOAc-PNC from 0.2 V to 0.8 V, suggesting a desirable four-electron ORR process (Fig. 3d and Table S3 in Supporting information). To further evaluate the ORR kinetics, the LSV curves for Fe-BOAc-PNC at 400~2025 rpm are tested in Fig. 3e. The K-L plots exhibit good linearity, indicating the corresponding ORR process conforms to the first-order reaction kinetics (Fig. 3f). The calculated average n value is 3.9 at 0.2–0.7 V, confirming it is a 4-electron ORR process. Tafel slope of Fe-BOAc-PNC is calculated to be 91 mV/dec, which is much lower than that of PNC (141 mV/dec), Fe-PNC (136 mV/dec), Fe-OAc-PNC (102 mV/dec), and Pt/C catalyst (96 mV/dec), implying its advanced electrode kinetics (Fig. 3g). To investigate the effect of "active point-conductive line-active point" connection on the charge transfer resistance, the EIS tests are performed with a frequency of 100 kHz–0.01 Hz. The arc diameter of Fe-BOAc-PNC is the smallest among all the catalysts, suggesting a faster charge transfer rate (Fig. 3h). The C_{dl} is evaluated through the CV plots from 5 mV/s to 50 mV/s within 1.065–1.165 V (Fig. S4 in Supporting information). Fe-BOAc-PNC reveals the C_{dl} value of 52.2 mF/cm^2,

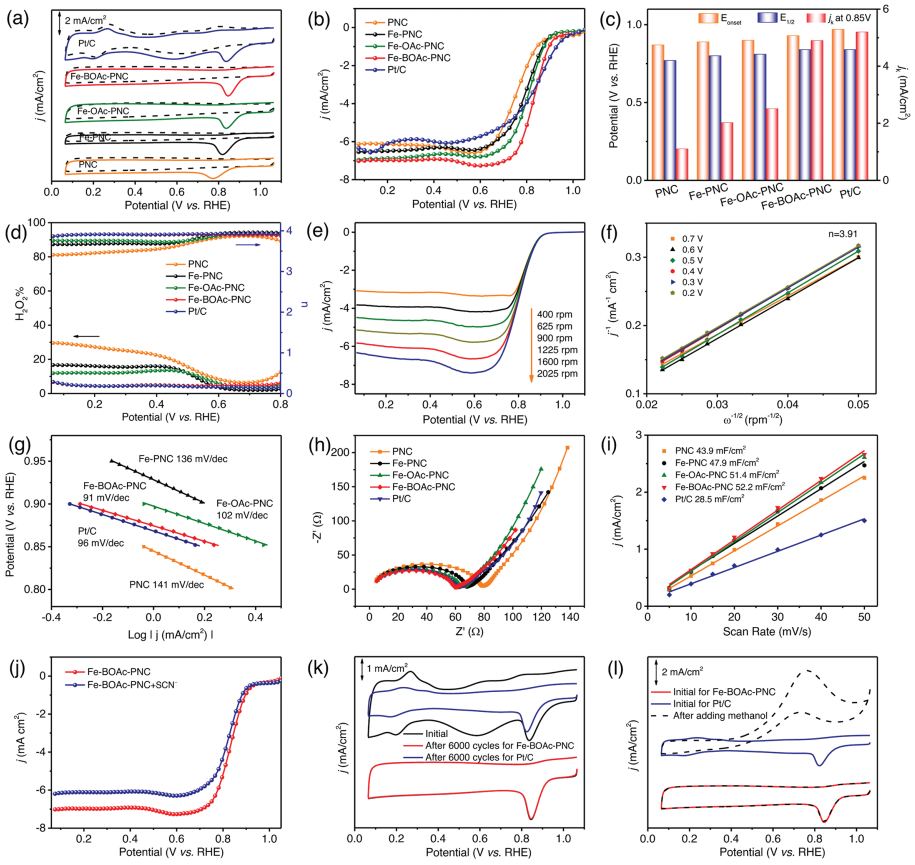

Fig. 3. Electrocatalytic ORR performance in 0.1 mol/L KOH electrolyte: (a) CV curves. (b) LSV curves at 1600 rpm. (c) The E_{onset}, $E_{1/2}$ and j_K at 0.85 V. (d) Electron transfer numbers and H_2O_2 yields. (e) LSV curves of Fe-BOAc-PNC at different rotating speeds. (f) K-L plots at different potentials. (g) Tafel plots. (h) Nyquist plots. (i) C_{dl} plots. (j) LSV curves of Fe-BOAc-PNC with/without 10 mmol/L KSCN. (k) Durability test. (l) Methanol tolerance test.

higher than those of PNC (43.9 mF/cm^2), Fe-PNC (47.9 mF/cm^2), Fe-OAc-PNC (51.4 mF/cm^2), and Pt/C catalyst (28.5 mF/cm^2), suggesting more active sites/surface area obtained for Fe-BOAc-PNC (Fig. 3i). Furthermore, the $E_{1/2}$ and current density of Fe-BOAc-PNC significantly decrease after injecting 10 mmol/L KSCN into the electrolyte, indicating isolated Fe-N_x active sites play a significant role towards ORR (Fig. 3j) [31]. More importantly, the stability and methanol tolerance measurements are evaluated because these two properties will significantly affect the practical application of the catalyst. As shown in Fig. 3k, Fe-BOAc-PNC exhibits slighter losses of potential and current through continuous 6000 CV cycles than Pt/C catalyst, suggesting its better stability. To verify the good stability of Fe-BOAc-PNC, the SEM and TEM images after 6000 CV cycles were observed. As shown in Fig. S5 (Supporting information), it is encouraging that Fe-BOAc-PNC remains the structure of hierarchically porous carbon interlinked CNTs after 6000 CV cycles, suggesting the prominent stability. In Fig. 3l, Fe-BOAc-PNC exhibits almost unchanged CV curves after injecting 3 mol/L methanol into 0.1 mol/L KOH media, while Pt/C electrode appears a reversed peak, signifying that Fe-BOAc-PNC has the excellent methanol resistance. According to the survey, the ORR performance of Fe-BOAc-PNC is comparable to that of some recently reported catalysts (Table S4 in Supporting information). The admirable electrocatalytic ORR performance for Fe-BOAc-PNC may be attributed to the following aspects: (1) Fe ions are doped through the Fe-imidazole coordination with the direct substitution of Zn ions and coordination with unsaturated Zn sites through the organic carboxylate linker, resulting in dense Fe-N_x active sites in the final pyrolyzed Fe/N-CCNTs. (2) The hexatomic carbon rings in organic carboxylate can efficiently lower the cyclization energy barrier of CNT formation, which is conductive to more entangled CNTs. (3) Such "active point-conductive line-active point" connections can effectively integrate highly conductive CNTs and active sites, thereby facilitating smooth mass transport and utilization efficiency of active sites. Actually, the formation of CNTs for PNC, Fe-PNC, Fe-OAc-PNC and Fe-BOAc-PNC is based on the self-catalyzed effect. Firstly, Fe species precipitate on the surface of carbon skeleton during high-temperature treatment to produce Fe nanoparticles. Next, Fe nanoparticles with high catalytic activity can catalyze the decomposition of carbon components in the MOFs to form CNTs. Finally, the Fe nanoparticles are enclosed in the grown CNTs [30]. However, some ligands such as MOF materials have high cyclization energy barriers of CNTs and/or lower carbon content. Thus, in order to obtain high yield and high-quality CNTs, some additional carbon sources need to be added. As for Fe-OAc-PNC, the hexatomic carbon rings of organic carboxylate can not only served as carbon sources, but also lower cyclization energy barrier for CNT formation [27]. Thus, the well-grown CNTs are generated for Fe-OAc-PNC. It is worth noting that the organic carboxylate plays essential roles on ORR performance, which are reflected in the following aspects: (1) Fe ions can be additionally doped in ZIF-8 precursors through the coordination with unsaturated Zn sites *via* organic carboxylate as linkers except the direct substitution of Zn ions with Fe ions, thus resulting in high-density Fe-N_x active sites after high-temperature pyrolysis. (2) More entangled CNTs can be generated because the six-atom carbon ring in sodium benzoate is capable of lowering the cyclization energy barrier during the CNT formation process. The produced CNTs ensure the rapid transport

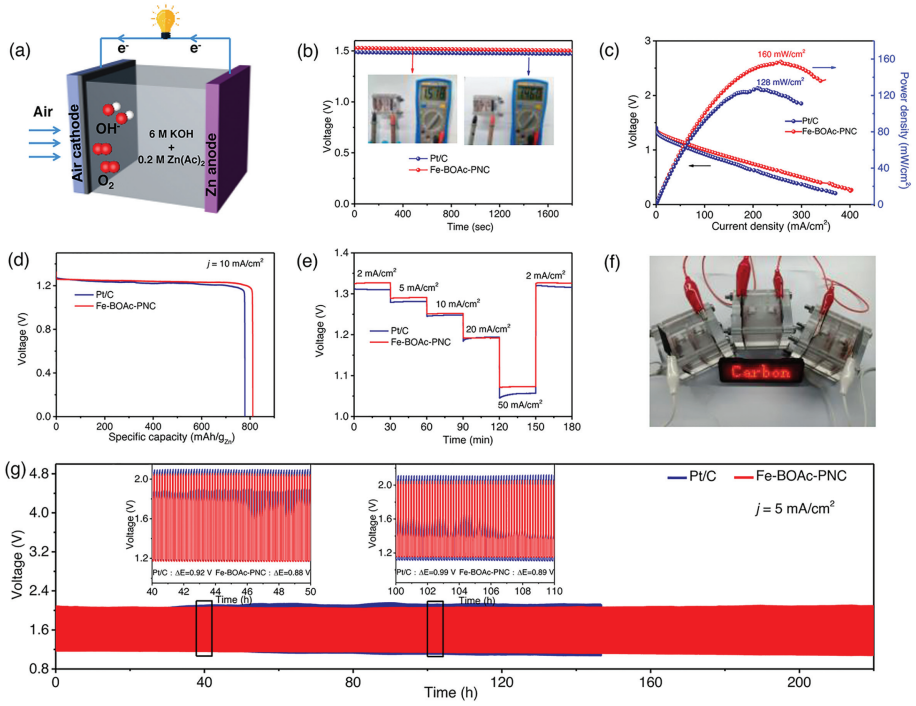

Fig. 4. (a) Schematic configuration of the primary ZAB. (b) OCV plots and photographs. (c) Polarization and power density curves. (d) Discharge curves at 10 mA/cm^2. (e) Discharge curves at different current densities. (f) Three Fe-BOAc-PNC-based ZABs in series to illuminate the LED screen. (g) Long-term charge-discharge curves at 5 mA/cm^2.

of reactants and products (OOH*, OH*, OH^-, H_2O, *etc.*) in the ORR process, thus increasing the catalytic activity. (3) The framework of Fe, N co-doped porous carbon interlinked CNTs has excellent thermal stability and effectively avoids the collapse of pore structures, which can improve the structural stability of the catalytic materials.

A homemade liquid ZAB has been fabricated inspired by promising ORR performance. A polished Zn plate, carbon paper coated Fe-BOAc-PNC or Pt/C catalyst and a mixed solution of 6.0 mol/L KOH and 0.2 mol/L $Zn(Ac)_2$ are used as the anode, the air cathode and the electrolyte, respectively (Fig. 4a). Fig. 4b illustrates that the liquid ZAB with Fe-BOAc-PNC delivers an open-circuit voltage (OCV) of 1.52 V, superior to the Pt/C based ZAB (1.46 V). As shown in Fig. 4c, Fe-BOAc-PNC based ZAB generates satisfying peak power density of 160 mW/cm^2, exceeding Pt/C based ZAB and recently reported catalysts (Table S5 in Supporting information).

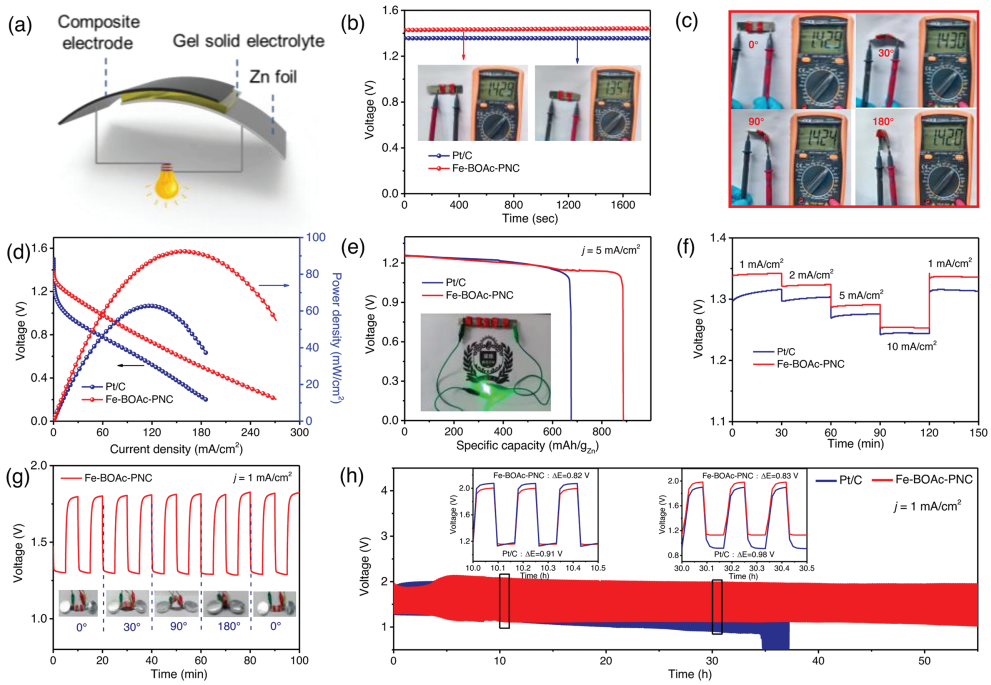

Fig. 5. (a) Diagram of the flexible ZAB. (b) The OCV plots and photographs. (c) The photographs of OCV for Fe-BOAc-PNC-based ZAB under different bending angles. (d) Discharge curves and power density plots. (e) Discharge curves at 5 mA/cm^2 (inset is the photograph of two Fe-BOAc-PNC-based ZABs in series to illuminate the LED light). (f) Discharge curves. (g) Discharge-charge cycling curves under different bending states. (h) Cyclic stability at 1 mA/cm^2.

The specific capacity of Fe-BOAc-PNC based ZAB (812 mAh/g) is higher than that of Pt/C driven ZAB (780 mAh/g) based on the mass of consumed Zn (Fig. 4d). Moreover, the ZAB assembled with Fe-BOAc-PNC possesses a slighter voltage drop than ZAB assembled with commercial Pt/C catalyst under different current densities (2–50 mA/cm^2), implying an outstanding rate capability (Fig. 4e). As a demonstration for practical application, Fig. 4f illustrates three ZABs with Fe-BOAc-PNC in series can illuminate a 3.7 V light-emitting diode (LED) screen. Furthermore, a cycling test is conducted to evaluate the charge and discharge cycling stability of ZABs (Fig. 4g). Specifically, the voltage gap of Fe-BOAc-PNC based ZAB during 40–50th h is 0.88 V, which is 40 mV smaller than that of Pt/C based ZAB (0.92 V). After continuous 60 h cycling, the voltage gap of ZAB with Fe-BOAc-PNC has almost no change. However, the voltage gap of ZAB with Pt/C exhibits an observable increase of 70 mV. These results confirm that the ZABs assembled with Fe-BOAc-PNC reveals excellent capacity and stability.

To further explore potential application for Fe-BOAc-PNC catalyst in wearable electronic devices, a flexible rechargeable ZAB has been assembled with the air electrode (Fe-BOAc-PNC or Pt/C catalyst loaded on composite electrode), an alkaline solid electrolyte and a polished Zn plate (Fig. 5a). The flexible ZAB based on Fe-BOAc-PNC delivers an OCV (1.43 V) (Fig. 5b), higher than that of the ZAB with Pt/C (1.35 V). Furthermore, the OCV of ZAB assembled with Fe-BOAc-PNC has no obvious change under different bending angles, indicating an excellent mechanical flexibility (Fig. 5c). As depicted in Fig. 5d, the peak power density of Fe-BOAc-PNC based flexible ZAB (93 mW/cm^2) is higher than those of Pt/C based ZABs (64 mW/cm^2) and recently reported non-noble catalysts (Table S6 in Supporting information). The specific capacity of ZAB with Fe-BOAc-PNC ups to 890 mAh/g at 5 mA/cm^2, outperforming the ZAB with Pt/C (675 mAh/g) (Fig. 5e). The series-connected Fe-BOAc-PNC based flexible ZABs can successfully power a green LED light (inset of Fig. 5e), demonstrating its practical applicability. The galvanostatic discharge plots at various current densities for Fe-BOAc-PNC-based ZAB exhibit steady voltage platform compared to the ZAB with Pt/C catalyst (Fig. 5f). Moreover, the flexible ZAB assembled with Fe-BOAc-PNC demonstrates a stable charge-discharge cycle under different bending angles at 5 mA/cm^2, fully illustrating its good foldability (Fig. 5g). The long-term cycle stability of ZABs assembled with Fe-BOAc-PNC and Pt/C is further evaluated by charge-discharge measurement at 5 mA/cm^2 (Fig. 5h). As depicted in the inset of Fig. 5h, the ZAB based on Fe-BOAc-PNC yields a voltage gap of 0.82 V (an initial discharge voltage of 1.17 V and charge voltage of 1.99 V), and there was only a slight voltage change over a 20 h period. Obviously, the Pt/C based ZAB is harshly deteriorative from the initial 0.91 V to 0.98 V after the same time, confirming the excellent durability of Fe-BOAc-PNC in the flexible ZAB. The favorable battery performances are mainly attributed to the hierarchically porous carbon interlinked CNTs with high-density and sufficiently exposed Fe-N_x active sites in Fe-BOAc-PNC.

In summary, the Fe, N co-doped hierarchically porous carbon interlinked CNTs with sufficiently exposed and high-density active sites have been prepared based on the self-catalyzed effect through the organic carboxylate-assisted engineering. The existing forms of Fe ions include Fe-imidazole configuration and the coordination with unsaturated Zn sites through organic carboxylate as linkers, leading to high-density Fe-N_x sites after pyrolysis. Besides, the hexatomic carbon rings of organic carboxylate lower the cyclization energy barrier to produce more entangled CNTs. The "active point-conductive line-active point" connections between CNTs and active sites can promote sufficiently exposed active sites and smooth mass transport. The prepared Fe-BOAc-PNC displays admirable electrocatalytic ORR activity ($E_{onset} = 0.93$ V, $E_{1/2} = 0.84$ V, $j_K = 4.90$ mA/cm^2) in 0.1 mol/L KOH. The liquid-state ZAB assembled with Fe-BOAc-PNC delivers excellent rate capability, high peak power density of about 160 mW/cm^2, and long-term cycle durability over 160 h. Moreover, the as-assembled all-solid-state ZAB shows superb peak power density of approximately 93 mW/cm^2 and excellent durability at 0°∼180° bending conditions. This work offers the route for preparing high-performance Fe-N/C catalysts with high-density and sufficiently exposed active sites towards ORR for energy conversion devices.

Declaration of competing interest

The authors declare that they have no known competing financial interests or personal relationships that could have appeared to influence the work reported in this paper.

Acknowledgments

This work was supported by the National Natural Science Foundation of China (No. U1804255), and the Key Research & Development and Promotion Projects in Henan Province (Nos. 222102520038 and 212102210651).

Supplementary materials

Supplementary material associated with this article can be found, in the online version, at doi:10.1016/j.cclet.2022.107886.

References

[1] Y. Arafat, M.R. Azhar, Y. Zhong, et al., Adv. Energy Mater. 11 (2021) 2100514.
[2] M. Zhao, H. Liu, H. Zhang, et al., Energy Environ. Sci. 14 (2021) 6455–6463.
[3] Z. Chen, D. Higgins, A. Yu, et al., Energy Environ. Sci. 4 (2011) 3167–3192.
[4] J.N. Liu, C.X. Zhao, D. Ren, et al., Adv. Mater. 34 (2022) 2109407.
[5] S. Gao, X. Li, L. Li, et al., Nano Energy 33 (2017) 334–342.
[6] X. Li, B.Y. Guan, S. Gao, et al., Energy Environ. Sci. 12 (2019) 648–655.
[7] Y. Zheng, S. Chen, K.A.I. Zhang, et al., ACS Appl. Mater. Interfaces 13 (2021) 13328–13337.
[8] H. Li, S. Di, P. Niu, et al., Energy Environ. Sci. 15 (2022) 1601–1610.
[9] Y. Zhao, X. Li, X. Jia, et al., Nano Energy 58 (2019) 384–391.
[10] Y. Zhao, Y. Liu, Y. Chen, et al., J. Mater. Chem. A 9 (2021) 18251–18259.
[11] Y. Wang, R. Gan, Z. Ai, et al., Carbon 181 (2021) 87–98.
[12] L. Zong, X. Chen, S. Dou, et al., Chin. Chem. Lett. 32 (2021) 1121–1126.
[13] Z.Y. Mei, S. Cai, G. Zhao, et al., Energy Storage Mater. 50 (2022) 12–20.
[14] Y. Zhu, B. Zhang, X. Liu, et al., Angew. Chem. Int. Ed. 53 (2014) 10673–10677.
[15] U.I. Kramm, J. Herranz, N. Larouche, et al., Phys. Chem. Chem. Phys. 14 (2012) 11673–11688.
[16] N. Ramaswamy, U. Tylus, Q. Jia, et al., J. Am. Chem. Soc. 135 (2013) 15443–15449.
[17] Y. Huang, K. Liu, S. Kan, et al., Carbon 171 (2021) 1–9.
[18] J. Yang, J. Hu, M. Weng, et al., ACS Appl. Mater. Interfaces 9 (2017) 4587–4596.
[19] R. Zhong, C. Zhi, Y. Wu, et al., Chin. Chem. Lett. 31 (2020) 1588–1592.
[20] H. Zhao, Y. Zhang, L. Li, et al., Chin. Chem. Lett. 32 (2021) 140–145.
[21] H. Wu, J. Wu, Y. Li, et al., Chem. Eng. J. 431 (2022) 134084.
[22] S. Yang, X. Xue, X. Liu, et al., ACS Appl. Mater. Interfaces 11 (2019) 39263–39273.
[23] Y. Song, Y. Peng, S. Yao, et al., Chin. Chem. Lett. 33 (2022) 1047–1050.
[24] H. Zhang, S. Hwang, M. Wang, et al., J. Am. Chem. Soc. 139 (2017) 14143–14149.
[25] Q. Lai, L. Zheng, Y. Liang, et al., ACS Catal. 7 (2017) 1655–1663.
[26] Y. Ye, F. Cai, H. Li, et al., Nano Energy 38 (2017) 281–289.
[27] X. Wang, A. Dong, Y. Hu, et al., Chem. Commun. 56 (2020) 10809–10823.
[28] B. Liu, H. Zhou, H. Jin, et al., Chin. Chem. Lett. 32 (2021) 535–538.
[29] L. Chai, Z. Hu, X. Wang, et al., Carbon 174 (2021) 531–539.
[30] J. Zhang, Y. Chen, Y. Liu, et al., Sci. China Mater. 65 (2022) 653–662.
[31] F. Zhou, P. Yu, F. Sun, et al., J. Mater. Chem. A 9 (2021) 6831–6840.
[32] Z. Xing, Y.P. Deng, S. Sy, et al., Nano Energy 65 (2019) 104051.
[33] Y. He, H. Guo, S. Hwang, et al., Adv. Mater. 32 (2020) 2003577.
[34] X. Zhao, X. Yang, M. Wang, et al., Appl. Catal. B 279 (2020) 119400.
[35] M. Tian, Y. Zhu, Y. Chen, et al., Nano Energy 83 (2021) 105825.
[36] Q. Tian, F. Xiao, H. Zhao, et al., Appl. Catal. B 272 (2020) 119039.
[37] H.W. Liang, W. Wei, Z.S. Wu, et al., J. Am. Chem. Soc. 135 (2013) 16002–16005.
[38] C.E. Szakacs, M. Lefevre, U.I. Kramm, et al., Phys. Chem. Chem. Phys. 16 (2014) 13654–13661.
[39] A. Zitolo, V. Goellner, V. Armel, et al., Nat. Mater. 14 (2015) 937–942.
[40] Y. Su, Y. Zhu, H. Jiang, et al., Nanoscale 6 (2014) 15080–15089.
[41] H.J. Qiu, P. Du, K. Hu, et al., Adv. Mater. 31 (2019) 1900843.